RSC Advances

PAPER

View Article Online
View Journal | View Issue

Cite this: *RSC Adv.*, 2025, **15**, 32284

Exploring allosteric properties of mammalian ALOX15: octyl (*N*-(4-(benzofuran-2-yl)-2-methoxyphenyl)sulfamoyl)- and octyl (*N*-(4-(1*H*-indol-2-yl)-2-methoxyphenyl)sulfamoyl) carbamates as ALOX inhibitors

Viktor Gavrilyuk, [a] Alejandro Cruz, [b] Vladislav Aksenov, [a] Danila Nurgaliev,[a] Alexander Zhuravlev, [a] Alexey Golovanov, [a] José M. Lluch, [c] Hartmut Kuhn, [d] Igor Ivanov *[a] and Àngels González-Lafont *[c]

Mammalian ALOX15 are allosteric enzymes but the mechanism of allosteric regulation remains a matter of discussion. Octyl (*N*-(5-(1*H*-indol-2-yl)-2-methoxyphenyl)sulfamoyl)carbamate inhibits the linoleate oxygenase activity of ALOX15 at nanomolar concentrations, but oxygenation of arachidonic acid is hardly affected. The mechanism of substrate selective inhibition suggests inter-monomer communication within the allosteric ALOX15 dimer complex, in which the inhibitor binding to monomer A induces conformational alterations in the structure of the active site of monomer B. Interactions of the NH-group of the indole moiety with the Fe(III)–OH^- cofactor or of the SO_2 group of the sulfocarbamate moiety with the side chain NH_2 group of Gln596 may be important for proper inhibitor placement in the ALOX15 allosteric complex. Substitution of a H-bond donor to a H-bond acceptor (NH–O-exchange) impacts but does not eliminate the ability of the compound to inhibit preferentially the LA-oxygenase activity of ALOX15. In contrast, swapping the positions of CH_3O- and NH groups at the 2-aryl moiety led to a loss of substrate selective inhibition. *In silico* docking studies and molecular dynamics-simulations using a dimeric allosteric ALOX15 model have shown that binding of the substrate molecule to ALOX15 monomer B may alter the structure of the monomer A-inhibitor complex forcing the inhibitor to adopt a different binding mode. Taken together, this data suggests the possibility of two-way communication between ALOX15 monomers during enzymatic catalysis.

Received 23rd May 2025
Accepted 28th August 2025

DOI: 10.1039/d5ra03640b

rsc.li/rsc-advances

1. Introduction

Arachidonic acid 15-lipoxygenase (ALOX15) is highly expressed in reticulocytes of mammals, and has been implicated in cell differentiation,[1,2] atherogenesis,[3,4] ferroptosis,[5] insulin resistance, and obesity.[6,7] ALOX15-derived metabolites of free polyenoic fatty acids have previously been identified as PPAR-γ ligands with strong anti-proliferative activity.[8] Moreover, an anti-inflammatory and tissue-protective role of arachidonic acid-derived ALOX15 metabolites has also been suggested.[9,10] Elucidation of the putative roles of ALOX15 metabolites derived from different polyunsaturated fatty acids made this enzyme a target for pharmacological research.

Human and rabbit ALOX15 orthologs utilize both linoleic (LA) and arachidonic (AA) acids as substrates and exhibit a dual positional specificity when oxygenating free AA to variable amounts of 15(*S*)–H(p)ETE and 12(*S*)–H(p)ETE.[11,12] Instead, 13(*S*)–H(p)ODE is the major metabolite of LA formed by the enzyme. The rate-limiting step of ALOX-catalysed PUFA oxygenation is the C–H activation of the substrate's bisallylic methylene group involved in the initial hydrogen abstraction.[13] For the human enzyme, the LA and AA oxygenation products, 13(*S*)–H(p)ODE and 12(*S*)–H(p)ETE, respectively, have been identified as allosteric effectors. Binding of either 13(*S*)–H(p)ODE or 12(*S*)–H(p)ETE to ALOX15 strongly altered the $[k_{cat}/K_M]^{AA}/[k_{cat}/K_M]^{LA}$ ratio in favour of AA oxygenation.[14] Additionally, for several ALOX15 inhibitors[15,16] different potencies against inhibition of AA and LA oxygenation have also been shown and all these data suggest an allosteric mechanism of their action.

[a]*Lomonosov Institute of Fine Chemical Technologies, MIREA – Russian Technological University, Vernadskogo pr. 86, Moscow, 119571, Russia. E-mail: ivanov_i@mirea@ru*
[b]*Department of Chemical Engineering-ETSEIB, Universitat Politècnica de Catalunya, Barcelona, 08028, Spain*
[c]*Departament de Química, Universitat Autònoma de Barcelona, Bellaterra, 08193, Barcelona, Spain. E-mail: angels.gonzalez@uab.cat*
[d]*Department of Biochemistry, Charite – University Medicine Berlin, Corporate member of Free University Berlin, Humboldt University Berlin and Berlin Institute of Health, Charitéplatz 1, Berlin, D-10117, Germany*

In the crystal structure, rabbit ALOX15 (PDB 2P0M) is present as a dimer that is composed of two conformationally different monomers.[17] In aqueous solutions rabbit ALOX15 may occur in an equilibrium between monomeric and dimeric fractions as indicated by small angle X-ray scattering measurements.[18] Although the molecular basis of the allosteric character of ALOX15 remains a matter of discussion, inter-monomer communication within the ALOX15 dimer has been suggested.[19] One of the scenarios of allosteric regulation suggests that ligand (inhibitor or activator) binding at the binding pocket of monomer A may induce conformational alterations in the structure of the substrate-binding cavity of monomer B[19] affecting the rate constants of the rate limiting C–H activation.

In previous studies we found that 5-(4-methoxyphenyl)-1*H*-indole-(**I**)[16] or 5-(4-methoxyphenyl)-1*H*-imidazole-(**II**)[20] derivatives (Fig. 1A) drastically reduced the linoleate oxygenase activity of rabbit and human ALOX15 at nano molar concentrations. Interestingly, at such low concentrations oxygenation of AA was hardly affected. As indicated by molecular dynamics (MD) simulations, both 5-(4-methoxyphenyl)-1*H*-indole and 5-(4-methoxyphenyl)-1*H*-imidazole derivatives were rigidly bound in the substrate binding cavity of ALOX15 monomer A and induced pronounced alterations in the structure of the hydrophobic inter-monomer interface. These structural alterations were further translated to the structure of the substrate-binding cavity of monomer B,[16,20] which might impact substrate fatty acid binding and/or the oxygenation reaction. Despite the differences in the structures of the inhibitor I or II (Fig. 1A) complexes with ALOX15,[16,20] the main interactions between the monomer A and the inhibitors, determined by MD simulations, were similar and two major interactions have been suggested:[20] (i) a hydrogen bond between the Fe(III)–OH^--cofactor and the NH-group of the indole or the imidazole moiety and (ii) a hydrogen bond between the side chain NH_2-group of Gln596 and the SO_2-groups of the corresponding sulfonamide or sulfocarbamate moiety.

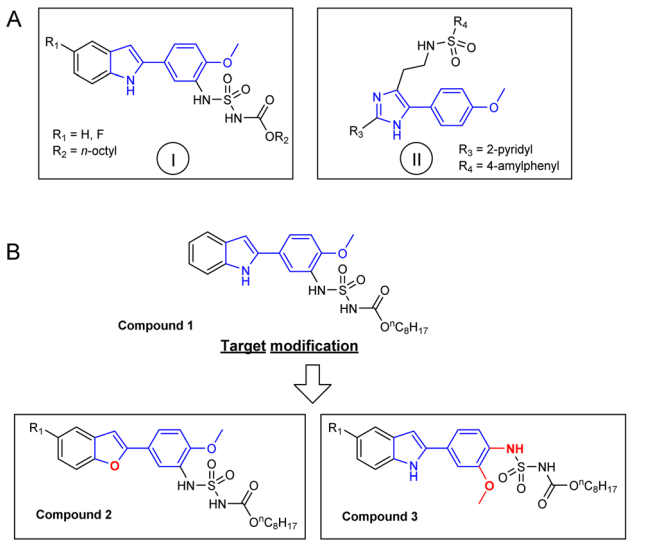

Fig. 1 Structure of selective inhibitors of the linoleate–oxygenase activity (A) and targeted modifications of compound **1** (B).

Unfortunately, it has never been explored whether these interactions play a role for proper positioning of the inhibitor in the allosteric ALOX15 complex and whether substrate binding at monomer B may induce an opposite effect on the structure of the inhibitor-monomer A-complex.

Site-directed mutagenesis studies are not helpful to answer these questions since alterations in the iron ligand sphere or Gln596 lead to either complete or partial inactivation of the enzyme.[21,22]

To investigate the mechanism of inhibitor binding in the allosteric ALOX15 complex we synthesized two structural analogues of the indole **1**, the benzofuran **2** and indole **3** (Fig. 1B). The later compound involved a swapped locations of CH_3O- and NH-groups at the benzene ring. An exchange of the indole to benzofuran moiety in compound **2** converts a H-bond donor to acceptor and, thus, this modification might affect inhibitor binding. On the other hand, preliminary docking studies of compound **3** inside the active site of ALOX15 monomer A suggested a loss of original interactions observed previously for compound **1** (Table S1) and, thus, a loss of its inhibitory activity was expected. Furthermore, in this work we compared the inhibitory potencies of newly synthesized compounds **2** and **3** against pure recombinant rabbit ALOX15 and investigated the mechanism of inhibition. Finally, we performed MD simulations using an allosteric enzyme model, in which the inhibitor occupies the substrate-binding pocket of monomer A, whereas monomer B binds the substrate fatty acid at its catalytic centre.

2. Result and discussion

2.1 Synthesis of octyl (*N*-(4-(benzofuran-2-yl)-2-methoxyphenyl)-sulfamoyl)carbamate (2)

Like the indole compound **1**,[16] the benzofuran **2** was obtained by a Fischer cyclization reaction under acidic conditions. Unlike the classical methods for preparation of 2-substituted indoles, in which the intermediate *N*-phenylhydrazone may be obtained by condensation of the phenylhydrazine with a corresponding ketone (Fig. 2, path A), the limited stability of *O*-phenylhydroxylamine suggested a need for an alternative path for preparation of *O*-phenylketoxime. Thus, *O*-phenylketoxime was prepared *via* *O*-arylation of the corresponding ketoxime by diphenyliodonim triflate (Fig. 2, path B; Scheme 1).

The synthesis of compound **2** is shown in Scheme 1. 4-Methoxy-3-nitroacetophenone (**4**) was used as the starting material. Its interaction with hydroxylamine hydrochloride led to oxime **5** in a quantitative yield. *O*-Arylation of **5** was carried out using diphenyliodonium triflate (**6**). Compound **6** was synthesized according to the protocol reported previously with some modifications.[23] *O*-Phenyl-1-(4-methoxy-3-nitrophenyl) ethan-1-one oxime **7** was prepared by the reaction of diphenyliodonium triflate **6** with oxime **5** in DMF in the presence of potassium *tert*-butoxide in a 74% yield.

The procedure for the cyclization of *O*-phenylketoximes described by Gao *et al.*[24] assumes consecutive application of a 4 M HCl solution in dioxane and 5 eq. of water. When we used a commercially available aqueous HCl solution (36%) 2-(4-

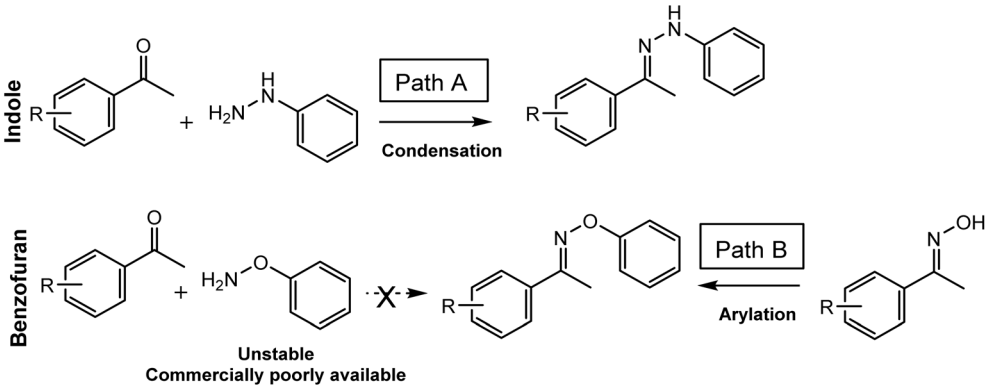

Fig. 2 Selection of synthetic strategy for preparation of compound 2.

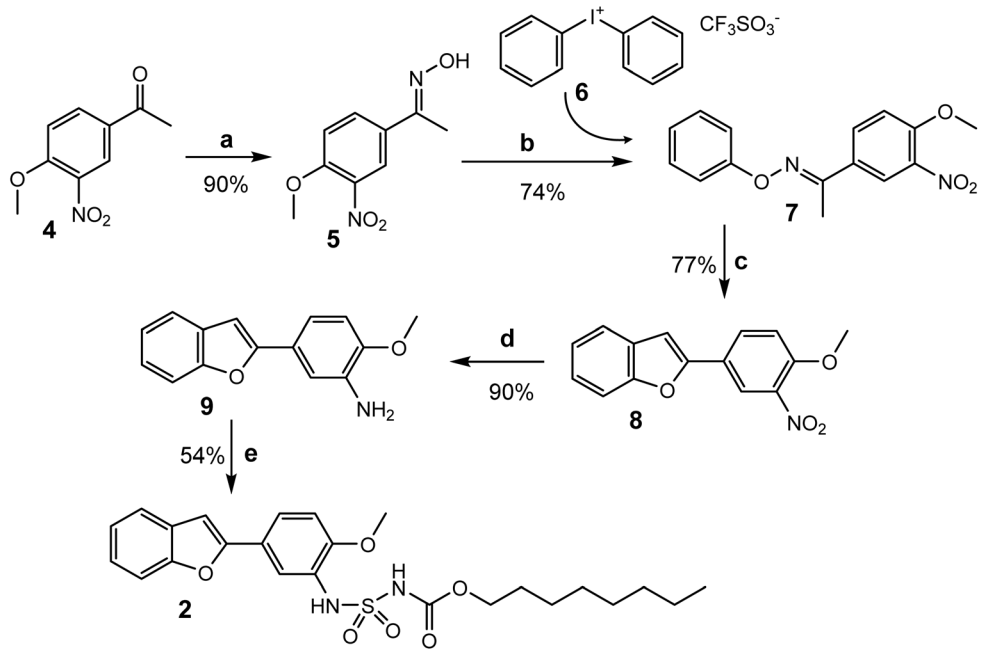

Scheme 1 Reaction conditions: (a) $NH_2OH \cdot HCl$, AcONa, aq. EtOH, reflux, 1 h; (b) diphenyliodonim triflate (6), ^{t}BuOK, DMF, rt, 1.5 h; (c) conc. HCl, dioxane, reflux, 5.5 h; (d) Fe, conc. HCl, MeOH, 60 °C, 3 h; (e) CSI, TEA, *n*-OctOH, DCM, rt, 3 h.

methoxy-3-nitrophenyl)benzofuran (**8**) was obtained in a 77% yield. The reduction of the nitro group of compound **8** was carried out with iron in the presence of HCl yielding 90% of 2-(3-amino-4-methoxyphenyl)-benzofuran **9**.

The target compound **2** was synthesized by reaction of compound **9** with chlorosulfonisocyanate and *n*-octanol in the presence of triethylamine as reported previously[16] and purified by preparative RP-HPLC to reach a ≥98% degree of purity.

2.2 Synthesis of octyl (*N*-(4-(1*H*-indol-2-yl)-2-methoxyphenyl)-sulfamoyl)carbamate (3)

The procedure for preparation of compound **3** is shown in Scheme 2. Ketone **15**, a key intermediate in the synthesis of the indole **3**, may be prepared from the corresponding chloro-anhydride **11** using the Grignard reaction, in which *N*-methoxymethylamine moiety serves as leaving group. Compound **12**, the so-called Weinreb amide, was obtained from the acid chloride **11** and *N*-methoxymethylamine in the presence of triethylamine. Unfortunately, during the reaction the nitro group of the Weinreb amide **12** was reduced yielding almost quantitively the side nitroso product **13**. This data was confirmed by GC-MS analysis. To avoid this problem an alternative synthetic path *via* diethylmalonate **14** was used. Diethylmalonate was converted to ethoxymagnesium malonate in the presence of magnesium ethylate followed by acylation of the intermediate with chloranhydride **11** to yield diethyl 2-(3-methoxy-4-nitrobenzoyl)malonate **14** in a one-pot procedure.

Decarboxylation of compound **14** in the presence of H_2SO_4 led to 3-nitro-4-methoxyacetophenone (**15**) in an 36.5% yield starting form anhydride **11**. Reduction of 3-nitro-4-methoxyacetophenone **15** by hydrogen in the presence of Pd/C

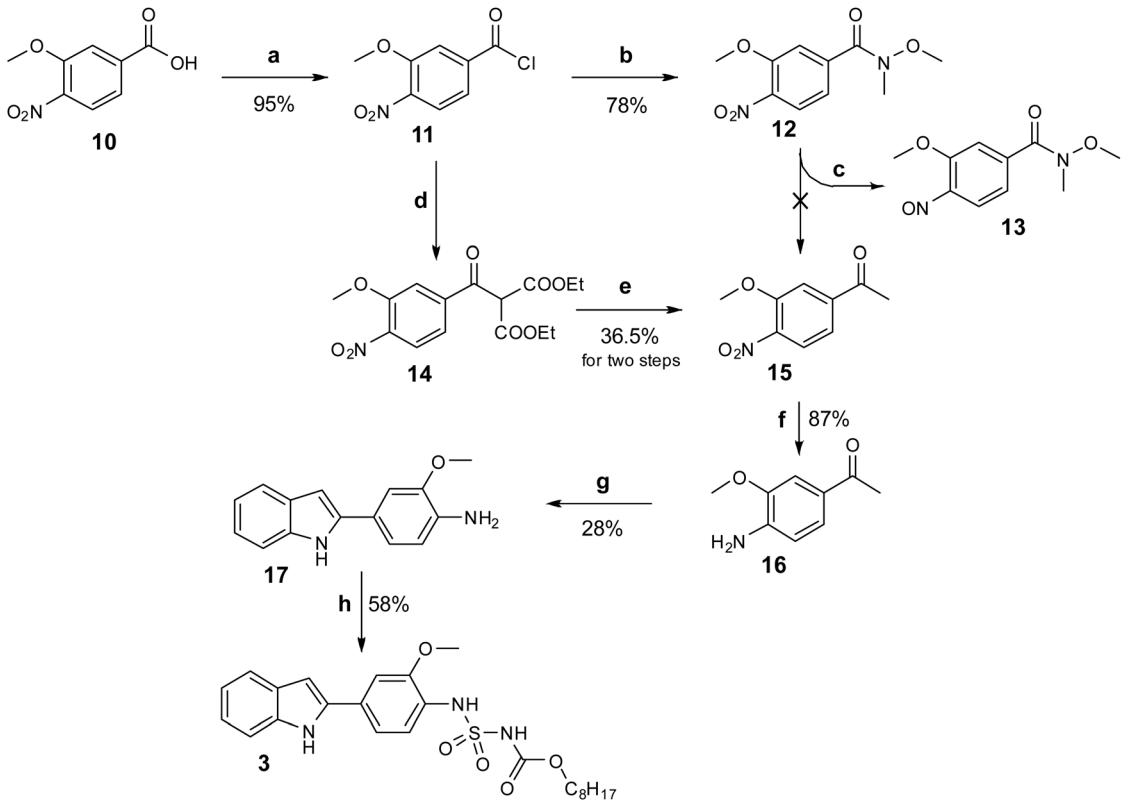

Scheme 2 Reaction conditions: (a) $SOCl_2$, DMF, toluene, reflux, 1 h; (b) MeNHOMe, TEA, DCM, rt, overnight; (c) MeMgI, THF, 0 °C, 1 h; (d) EtOOCCH(MgOEt)COOEt, Et_2O, reflux, 3 h; (e) H_2SO_4, AcOH, H_2O, reflux, 3.5 h; (f) Fe, conc. HCl, MeOH, 60 °C, 3 h; (g) phenylhydrazine, PPA, 130 °C, 20 min; (h) CSI, TEA, *n*-OctOH, DCM, rt, 3 h.

(10%) resulted in the formation of large amounts of the demethylation side-product so that only a moderate yield (39%) of the target amine **16** was obtained. Application of 5% Pd/C was not sufficient for any quantitative conversion of nitro compound **15**. Instead, using iron in the presence of HCl made it possible to obtain **16** in an 87% yield. The latter was used for the next synthetic step without further purification.

The indole **17** was prepared *via* path A according to the previously described protocol[16] (Fig. 2). The condensation of phenylhydrazine with ketone **16** *via* intermediate hydrazone followed by Fischer cyclization was carried out as one-step procedure in polyphosphoric acid. The target compound **3** was synthesized by reaction of **17** with chlorosulfonisocyanate and *n*-octanol in the presence of triethylamine and purified by preparative RP-HPLC to reach a ≥98% degree of purity.

2.3 Inhibitory potencies of compounds 2 and 3 against rabbit ALOX15

Inhibition was measured employing the standard spectrophotometric assay monitoring the rate of conjugated diene formation when arachidonic or linoleic acids were used as substrates. The IC_{50} values (Fig. 3A) of compound **2** were 0.42 ± 0.04 and 5.73 ± 0.18 μM for LA and AA oxygenation, respectively. This data indicates a moderate reduction in inhibitory potency and substrate specificity of compound **2** against LA oxygenation when compared with the reference compound **1** (IC_{50} 0.040 ± 0.001 and 2.06 ± 0.14 μM on LA and AA).[16] Comparison of the data indicates that NH–O exchange in the core pharmacophore decreases the substrate specificity. In fact, the IC_{50}(LA)/IC_{50}(AA) ratio changes from 0.02 obtained for the reference compound **1** to 0.07 for compound **2**. For compound **3** (Fig. 3C), which is a structural isomer of the reference compound **1**, we measured IC_{50} values of 19.51 ± 3.34 μM for LA and 16.08 ± 2.02 μM for AA oxygenation. This data indicated a complete loss of substrate specificity, but also a marked reduction of the inhibitory potency.

To explore the mode of inhibition we carried out extensive kinetic measurements (Fig. 3B and D) and the following kinetic constants were obtained for the oxygenation reaction in the absence of inhibitor: $k_{cat}^{LA} = 18.83 \pm 2.34\ s^{-1}$, $K_M^{LA} = 31.58 \pm 7.03$ μM or $k_{cat}^{AA} = 4.86 \pm 1.02\ s^{-1}$, $K_M^{AA} = 16.14 \pm 3.60$ μM for LA or AA oxygenation, respectively.

Although, the catalytic activity of this enzyme preparation (electrophoretic purity >95%, Fig. S1) was somewhat lower with AA than described previously, the K_M values are consistent with those from our previous reports[16] and the 15-HETE : 12-HETE ratio was 95 : 5 (Fig. S2).

Using LA as a substrate, compound **2** induced a marked decrease in k_{cat} but only a moderate reduction in the K_M-value (Fig. S3). For AA as substrate, compound **2** induced a marked decrease in the K_M-value, whereas k_{cat} was almost unaffected (Fig. S3). Finally, we fitted these inhibitor data to different inhibition models (Fig. 3B) and found that the best fits were

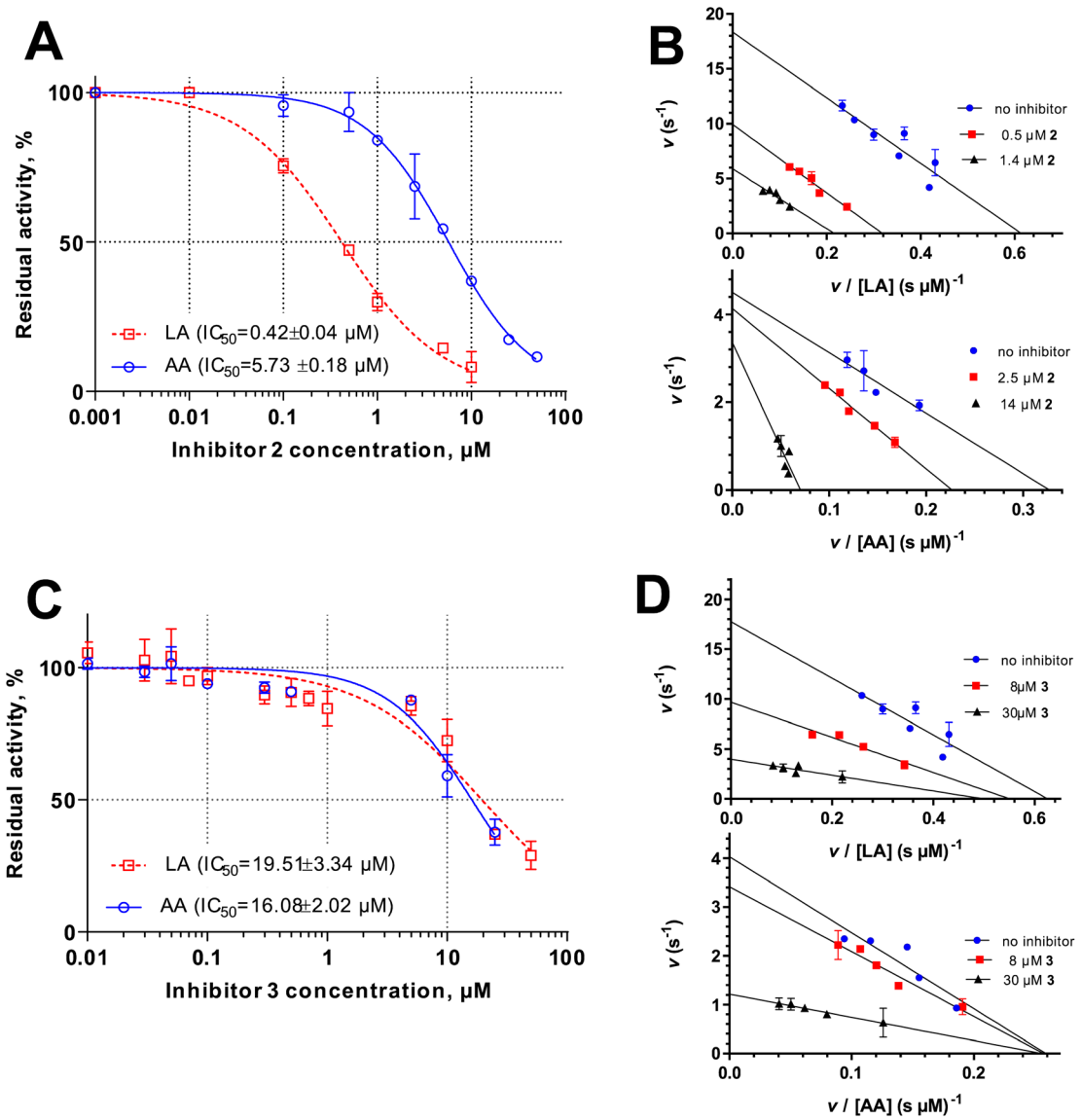

Fig. 3 Inhibitory potency of compounds **2** and **3** for rabbit ALOX15. (A) and (C) Dose response curves for inhibition of the LA- and AA-oxygenase activities of pure recombinant rabbit ALOX15 by compounds **2** and **3**. (B) and (D) Eadie–Hofstee plots demonstrating the effects of **2** and **3**, respectively, on rabbit ALOX15 when incubated with 25 μM arachidonic or linoleic acids. The data points represent means ± SEM with $n = 3$.

obtained for a model of a non-competitive inhibition of LA oxygenation with a K_i of 0.39 ± 0.02 μM ($R^2 = 0.986$). On the other hand, inhibition of AA oxygenation by compound **2** (Fig. 3B) could be equally well described using a mixed model of inhibition ($R^2 = 0.964$) tending to a competitive mode with a K_i of 4.45 ± 1.83 μM ($\alpha = 8.3$). In this case, the dissociation constant ratios Kd^{EI}/Kd^{ESI} of 0.1 for AA suggested a higher binding affinity of compound **2** to the empty enzyme (E) rather than to the enzyme–substrate complex (ES^{AA}).

Inhibition of LA and AA oxygenation by the compound **3** (Fig. 3D) could be equally well described by an uncompetitive mode of inhibition with a K_i of 7.41 ± 0.87 μM ($R^2 = 0.968$) for LA and K_i of 14.64 ± 3.14 μM ($R^2 = 0.915$) for AA. In this case, the inhibitor **3** induced a marked decrease in both k_{cat}- and K_M-values (Fig. S4). A reduction of both values suggests a better enzyme–substrate binding owing to constant depletion of the ES^{AA}-complex upon inhibitor binding (ESI^{AA} formation). This inhibition mode suggests that the inhibitor preferentially binds to the enzyme–substrate complex (ES^{AA}) rather than to the empty enzyme. A similar mode of inhibition was observed previously for the reference compound **1** when AA was used as a substrate.[16] In summary, one may conclude that compound **3** binds to allosteric ALOX15-substrate complex, but swapping the positions of the CH_3O- and the NH-groups abolishes the substrate selectivity of the inhibitory effect. Compound **3** has substantially lower inhibitor potency when compared with its analogue **1**.

2.4 MD simulations of enzyme–inhibitor complexes

To explain our experimental observations, we performed *in silico* docking calculations of compound **3** inside the substrate

binding cavity of monomer A of the dimeric rabbit ALOX15 crystal structure (PDB entry 2P0M). To perform a thorough conformational exploration of compound **3** inside this cavity, we calculated 1000 solutions which have been grouped into different clusters. In the highest-score complex (**3**(1):ALOX15), the 2-phenylindole ring is located inside the substrate binding cavity of monomer A with its OCH_3-group oriented towards Gly407. In contrast, the reference compound **1** was located deeper inside the cavity with the OCH_3-group oriented towards Phe175.[16] Both the sulfonamide moiety and the hydrophobic tail of the indole compound **3** are located at the entrance of the cavity of monomer A so that the 2-phenylindole core is far from the bottom of the substrate binding pocket. In the second-best score complex (**3**(2):ALOX15), the OCH_3-group is oriented towards the interior of the cavity, pointing towards Ile663, which is located at the end of the α18 helix of monomer A, whereas the OCH_3-group of the reference compound **1** points towards Phe175 that belongs to the α2 helix of monomer A.[16] In Fig. 4A and C, the two highest-score docking binding modes **3**(1):ALOX15 and **3**(2):ALOX15, respectively, are depicted. In addition, we have included a description of the main inhibitor:protein interactions in those complexes in the SI file. Remaining complexes, in which the 2-phenylindole ring is located either at the entrance or outside the cavity of monomer A, were not considered for further MD simulations.

Next, a 200 ns MD simulation was carried out for the two highest-score binding modes. After the MD simulation, the ring core of compound **3** in the **3**(1):ALOX15 complex penetrates more deeply into the cavity of monomer A. The aromatic ring of compound **3** forms numerous hydrophobic interactions with the side chains of amino acids lining the cavity, especially with Ala404, Leu408, Val409, Leu362, Leu597, Leu358 and Phe415, and forms a π–π interaction with His361, which is part of the coordination sphere of iron cofactor. The OCH_3-group of compound **3** is located parallel to the α2 helix and points towards the α18 helix of monomer A, which carries Gln596 (ref. 21) (not shown). In addition, the NH-group of the 2-phenylindole appears to interact with the $Fe(III)–OH^{2+}$ cofactor (Fig. 4B). The most significant interactions between the inhibitor and the enzyme protein in the **3**(1):ALOX15 complex are presented in Table 1. In the **3**(2):ALOX15 complex after the MD simulation, the ring core of compound **3** penetrates much deeper into the cavity of monomer A. Most significant interactions are presented in Fig. 4D and Table 1. As expected, the interaction of compound **3** with the ALOX15 dimer interface, arisen from a greater proximity and interaction of the OCH_3 group with the α18 helix of monomer A, triggers a "wall" formation for the **3**(2):ALOX15 complex, which prevents the anchoring of the carboxylate group of the corresponding substrate to Arg403 and Arg599 of monomer B (see below). However, the degree of blockage is lower than that observed previously for the reference complex of compound **1**.[16] Although the effects induced by the inhibitor in these two binding modes differ considerably, they could be relatively easily

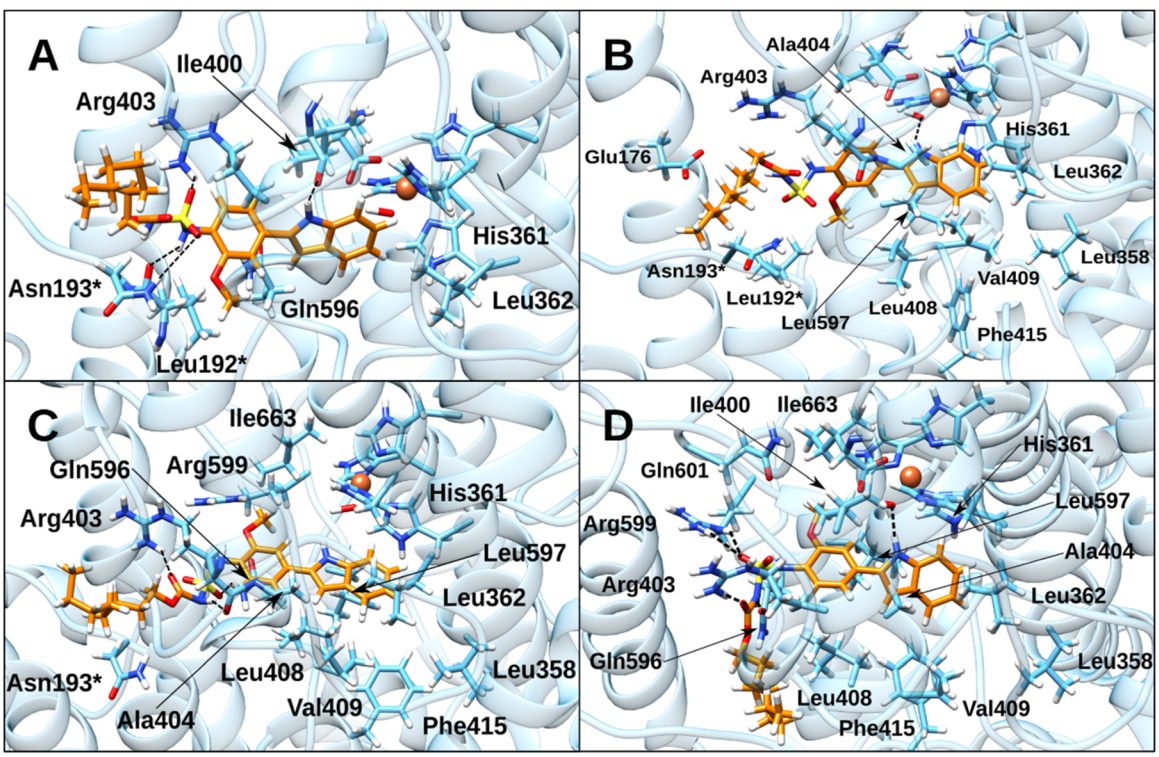

Fig. 4 Initial and stable binding modes of compound 3 (in orange) in complexes **3**(1):ALOX15 and **3**(2):ALOX15. The residues that interact with this compound have been represented, indicating with an asterisk the residues that belong to monomer B. For the sake of clarity, only hydrogen bonds have been represented with black dashed lines. (A) and (C) Best docking solution for the **3**(1):ALOX15 and **3**(2):ALOX15 complexes, respectively. In panel A, Leu362 has been depicted in order to show the position of the monomer A bottom. (B) and (D) The last frame of the 200 ns MD simulation corresponding to the **3**(1):ALOX15 and **3**(2):ALOX15 complexes, respectively.

Table 1 Most significant interactions that compound **3** forms in the last structure of the MD simulations for the **3**(1):ALOX15 and **3**(2):ALOX15 complexes. All interacting partners belong to monomer A unless otherwise indicated

Group	Type of interaction	Interaction partner	Distance, Å
		3(1):ALOX15 complex	
NH (indol)	Hydrogen bond	Fe(III)–**O**H$^-$	(*d*(**3**–H5–OH–Fe) = 2.398
	Unfavorable electrostatic	Fe(III)–O**H**$^-$	(*d*(**3**–H5–OH–Fe) = 2.469
OCH_3	Hydrophobic	Leu408 (sidechain)	
		Leu597 (sidechain)	
		Leu192(B) (sidechain)	
NH − SO_2 − NH	Unfavorable electrostatic	Arg403 (sidechain NH_2)	(*d*(**3**–H13–HH11–Arg403) = 3.121
S**O**$_2$	Electrostatic	Asn193(B) (sidechain NH_2)	(*d*(**3**–O2–HD22–Asn193) = 4.874
NH − SO_2 − **NH**	Electrostatic	Glu176 (sidechain)	*d*(**3**–H14–OE1–Glu176) = 5.028
	Unfavorable electrostatic	Arg403 (sidechain NH_2)	*d*(**3**–H14–OE2–Glu176) = 4.219
			d(**3**–H14–HH12–Arg403) = 3.614
C(O)O	Electrostatic	Arg403 (sidechain NH_2)	–[a]
C(**O**)O	Unfavorable electrostatic	Arg403 (backbone O)	*d*(**3**–O4–O–Arg403) = 3.633
		3(2):ALOXa5 complex	
NH (indol)	Hydrogen bond	Fe(III)–**O**H$^-$	*d*(**3**–H5–OH–Fe) = 1.977
OCH_3	Hydrophobic	Ile400 (sidechain)	
		Leu597 (sidechain)	
		Ile663 (sidechain)	
NH − SO_2 − NH	Electrostatic	Gln601 (sidechain CO)	*d*(**3**–H13–OE1–Gln601) = 4.589
	Unfavorable electrostatic	Arg599 (sidechain NH and NH_2)	*d*(**3**–H13–HE–Arg599) = 3.008
S**O**$_2$	Hydrogen bond	Arg599(sidechain NH)	*d*(**3**–O2–HH21–Arg599) = 2.138
			d(**3**–O2–HE–Arg599) = 2.024
NH − SO_2 − **NH**	Hydrogen bond	Gln596 (sidechain CO)	(*d*(**3**–H14–OE1–Gln596) = 1.941
C(**O**)O	Hydrogen bond	Arg403 (sidechain NH_2)	*d*(**3**–O4–HH11–Arg403) = 2.070

[a] Due to multiple interactions between Arg403 and the ester group, distances have not been indicated.

interconverted by a rotation of the benzene ring. However, our MD simulations of the **3**(1):ALOX15 and **3**(2):ALOX15 complexes indicate that both binding modes of compound **3** are stable since the interconversion between them has not been observed, indicating a non-negligible free energy barrier for such rotation process. The backbone RMSDs of ALOX15 dimer in **3**(1):ALOX15 and **3**(2):ALOX15 complexes are shown in Fig. S5. The RMSFs per residue of α2 and α18 helices in chain B are shown for both complexes in Fig. S6.

2.5 MD simulations of enzyme–inhibitor–substrate complexes

For both substrates, AA and LA, 1000 docking solutions have been calculated into the cavity of monomer B for each of the **3**(1):ALOX15 and **3**(2):ALOX15 complexes, using the final structures of their MD simulations as receptor. Only the results corresponding to the best cluster of AA and LA compatible with the reactivity observed for each of these substrates, *i.e.*, the best cluster in which AA or LA exhibit a reactive distance between the Fe(III)–OH^{2+} cofactor and the C13-AA or C11-LA, respectively, and at least one of hydrogen atoms of these carbon atoms is well oriented for their abstraction, are presented. As expected, in the **3**(1):ALOX15 complex, dockings of AA and LA into the cavity of monomer B of the ALOX15 dimer provide solutions of these substrates with the carboxylate group oriented towards the Arg403 and Arg599 site, since this is the customary COO-group orientation and there is no wall blocking that site. However, Gln596, Ser178 and Ser592 are in charge of the fixation of the substrate's carboxylate group (Fig. 5). These three residues belong to the dimer interface, particularly, Ser178 is located at the α2 helix of monomer B and Ser592-Gln596 pair is located at the α18 helix of this same monomer, while the carboxylate group of the substrate is located between these two α helices of monomer B. In relation to initial H abstraction, both LA and AA were expected to exhibit high reactivity since their reactive carbons, C11 and C13, respectively, have been located close to the Fe(III)–OH^{2+} cofactor (3.761 Å and 2.938 Å, respectively), whereby the reactivity of AA is favored since its C13 is closer to the cofactor and LA has poorly oriented hydrogens at C11 for such abstraction (Fig. 5). In contrast, the AA and LA carboxylate groups in the cavity of monomer B for the **3**(2):ALOX15 complex (Arg403 and Arg599 are blocked here, not shown) are oriented to the opposite side, as it was observed for the reference compound **1**. In this case, the residues involved in the anchoring of the substrate's carboxylate group are the same as those observed for the reference compound **1** (Asn152 and Arg405) (Fig. 5). In relation to H abstraction, both LA and AA were expected to exhibit high reactivity since both C11 of LA and C13 of AA have been located very close to the Fe(III)–OH^{2+} cofactor (3.541 Å and 2.938 Å, respectively), but reactivity of AA could be greater than that of LA since its C13 has a shorter distance to the cofactor and the C11 hydrogen atoms of LA are poorly oriented for their abstraction (Fig. 5). After MD simulations (200 ns) of the **3**(1):LA/AA:ALOX15 complexes, presence of either LA or AA in the cavity of monomer B induce significant reorganization of the inter-monomer interface of the ALOX15

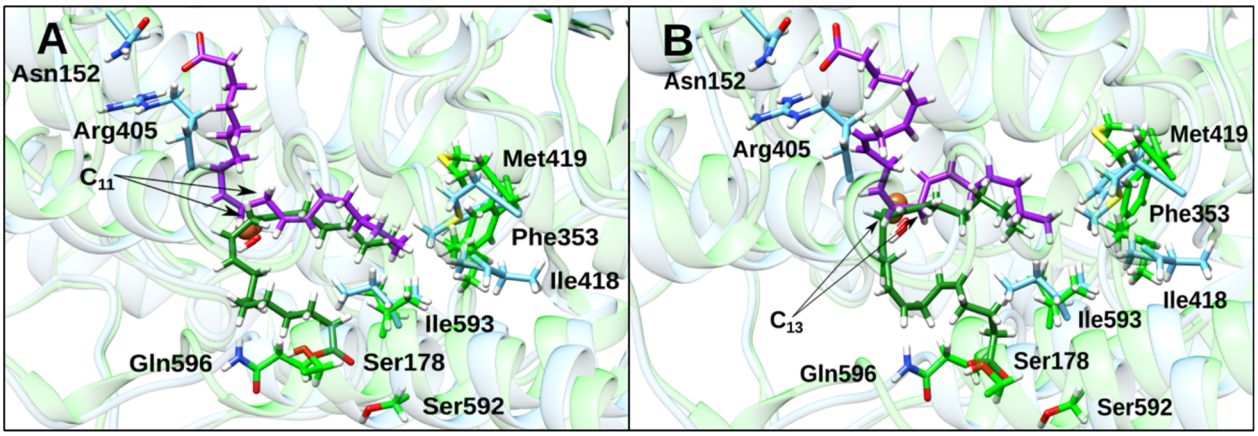

Fig. 5 (A) Binding modes of LA in monomer B according to docking calculations for **3**(1):ALOX15 and **3**(2):ALOX15 complexes (in dark green and purple, respectively). The residues that constitute the bottom of the cavity have been represented along with the residues that can become important for substrate fixation. (B) Binding modes of AA in monomer B according to docking calculations for **3**(1):ALOX15 and **3**(2):ALOX15 complexes (in dark green and purple, respectively). The residues that constitute the bottom of the cavity have been represented along with the residues that can become important for substrate fixation.

dimer (formed by the α2 and α18 helices of both monomers). The backbone RMSDs of ALOX15 dimer in **3**(1):LA/AA:ALOX15 and **3**(2):LA/AA:ALOX15 complexes are shown in Fig. S5. The RMSFs per residue of α2 and α18 helices in chain B are shown for those complexes in Fig. S6.

Formation of H bridges between the substrate's carboxylate-group and aforementioned interface residues (Ser178 of the α2 helix, and Ser592 and Gln596 of the α18 helix) involved in its fixation (Fig. 6A) induces displacement of the α2 and α18 helices of monomer B and this structural alteration is subsequently transmitted to the corresponding helices of monomer A. In this reorganization process the α18 helix of monomer A moves towards the interior of its cavity so that it drastically reduces the space available for the OCH_3-group of inhibitor **3** owing to the proximity to the side chain of Gln596 (Fig. 6B). This promotes a slight distancing of the ring core of **3** from the bottom of the cavity that allows rotation of the benzene ring, placing the OCH_3-group of **3** at the C-terminal end of the α18 helix. Therefore, the presence of substrate in the cavity of monomer B for the **3**(1):LA/AA:ALOX15 complexes triggers the conversion of the binding mode of inhibitor **3** observed in the **3**(1):ALOX15 complex to that of the **3**(2):ALOX15 complex through an inwards movement of α18 helix of monomer A. Once this conversion has taken place, the ring core of **3** returns to the bottom of the cavity and the OCH_3-group induces formation of a wall that blocks Arg403 and Arg599 in monomer B *via* its interaction with the α18 helix of monomer A. Thus, inhibition of both LA and AA oxygenation may occur only in the **3**(2):LA/

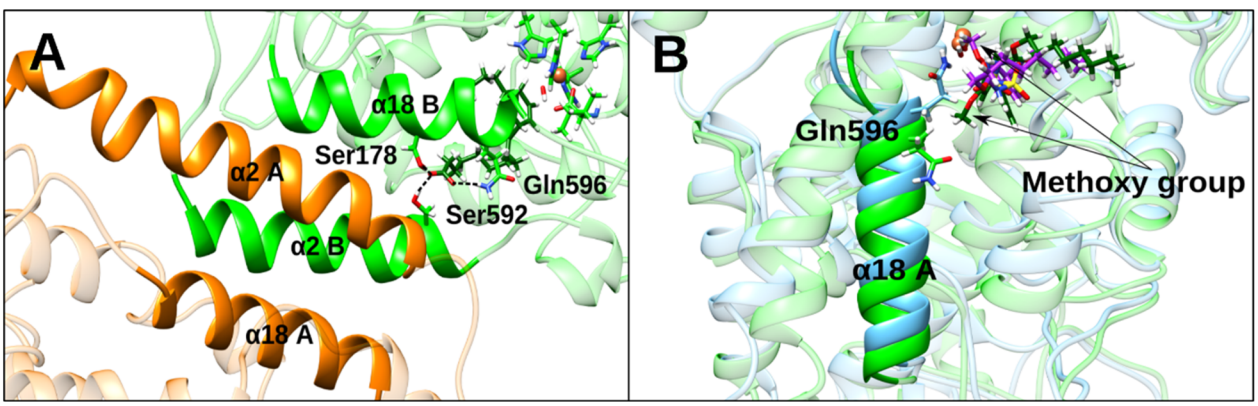

Fig. 6 (A) Representation of substrate anchoring in the **3**(1):LA:ALOX15 tertiary complex before dimer interface reorganization. In this figure, the substrate's carboxylate group (in dark green) anchors through hydrogen bonds with residues Ser178, Ser592, and Gln596, which belong to the interface α-helices of monomer B (highlighted in green). This interaction triggers the global reorganization of the α-helices in ALOX15's interface (highlighted in orange and green for monomers A and B, respectively). Notably, once the interface reorganizes, the substrate will be expelled. Hydrogen bonds are indicated by black dashed lines. (B) Representation of α18 helix displacement in monomer A. The α18 helix (highlighted in green and blue for before and after displacement, respectively) shifts inward due to the interface reorganization. The approach of Gln596 towards OCH_3-group of **3** induces a rotation of the benzene ring containing it, converting binding mode 1 to mode 2 (in dark green and purple, respectively).

AA:ALOX15 complexes since the **3**(1):LA/AA:ALOX15 complexes are converted to **3**(2):LA/AA:ALOX15 when the substrate is present in the cavity of monomer B. In the **3**(2):LA/AA:ALOX15 complexes, there is no significant effect on inhibitor induced by the substrates binding. Both substrates remain inside the cavity of monomer B, exhibiting poses similar to those found in docking calculations. These poses can be grouped into two distinct clusters (Fig. 7).

In one of the clusters, the substrate's carboxylate group is located slightly deeper at the cavity entrance (panels A and C in Fig. 7). For this cluster (cluster 1), residues Asn152 and Arg405 bind the carboxylate group, and the carbon atom that undergoes hydrogen abstraction is relatively far away from the Fe(III)–OH^{2+} cofactor. A similar observation was made for the substrates in the presence of the reference compound **1**. By contrast, in the other cluster with the more superficial carboxylate (cluster 2), which is stabilized by Lys146, the carbon atom which undergoes hydrogen abstraction is very close to the Fe(III)–OH^{2+} cofactor (panels B and D in Fig. 7). Notably, both clusters have similar populations, but despite their conformational similarity, cluster 1 may be associated with substrate inhibition, while cluster 2 with significant activation.

Regarding the reactivity of the considered substrates, we used evaluation criteria based on distances and well-oriented structures for hydrogen abstraction from the reactive carbon atoms and their corresponding hydrogen atoms. Since the oxygen atom of the Fe(III)–OH^{2+} cofactor is responsible for hydrogen abstraction and the reactive carbon atoms for LA and AA are C11 and C13, respectively, the distances *d*(C11–OH), *d*(H11proS–OH), and *d*(H11proR–OH) for LA, and *d*(C13–OH), *d*(H13proS–OH), and *d*(H13proR–OH) for AA have been considered. As previously defined in other works,[16,20] a well-oriented structure for hydrogen abstraction is one where at least one of the two hydrogen atoms from the corresponding reactive carbon atom is well-positioned for abstraction, *i.e.*, one or both hydrogen atoms are located closer to the oxygen atom of

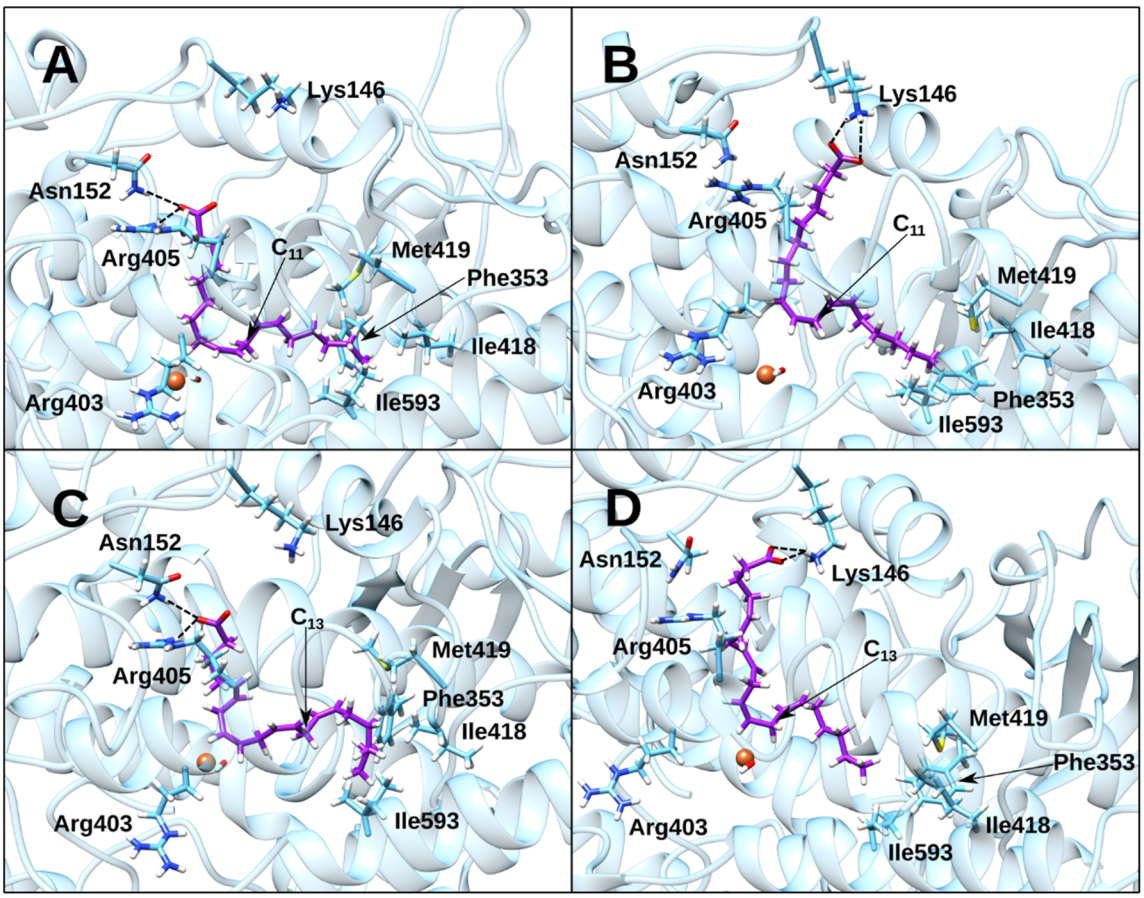

Fig. 7 Representation of the two binding modes observed for the substrates during MD simulations of the **3**(2):LA/AA:ALOX15 complexes (panels A and B for LA; panels C and D for AA). In cluster 1 (panels A and C), the substrate exhibits inactive position because the reactive carbon atom is distanced from the Fe(III)–OH^{2+} cofactor's oxygen atom. In cluster 2 (panels B and D), the substrate adopts an active conformation. Despite significant differences in reactivity, these binding modes are structurally very similar. The key distinction lies in the depth of the carboxylate group and the hydrophobic tail of the corresponding substrate within the cavity. This depth is determined by the specific residues that attach the carboxylate group. Specifically, for cluster 1, both the carboxylate group and the hydrophobic tail penetrate deeper into the cavity, with binding facilitated by Asn152 and Arg405. In contrast, for cluster 2, both groups penetrate less, and carboxylate binding is exclusively governed by Lys146. The position of the cavity bottom and the Fe(III)–OH^{2+} cofactor is indicated for spatial orientation. Additionally, the position of the reactive carbon atoms of the substrates are indicated to highlight the difference in reactivity for both binding modes. Hydrogen bonds are represented by black dashed lines.

Table 2 Relevant average distances for hydrogen abstraction and the percentage of well-oriented structures observed for LA during MD simulations of the LA:ALOX15, **3**(2):LA:ALOX15 and **1**:LA:ALOX15 complexes

System	$d(C_{11}–OH)$ (Å)	$d(H_{11proS}–OH)$ (Å)	$d(H_{11proR}–OH)$ (Å)	Percentage of well-oriented structures
Without inhibitor	4.6	4.7	4.6	90.09
3	4.8	4.8	5.0	81.55
1	5.5	6.2	5.6	34.00

the Fe(III)–OH^{2+} cofactor than the reactive carbon atom containing them.

Tables 2 and 3 contain the relevant average distances for hydrogen abstraction (d(C11–OH), d(H11proS–OH), and d(H11proR–OH) for LA, and d(C13–OH), d(H13proS–OH), and d(H13proR–OH) for AA) and the percentage of well-oriented structures observed during MD simulations of the **3**(2):LA/AA:ALOX15 complexes. For comparative purposes, the values of these magnitudes obtained from MD simulations of the LA/AA:ALOX15, and **1**:LA/AA:ALOX15 complexes have also been included.

According to the distance criteria, the data present in Tables 2 and 3 suggest that the ALOX15 selective inhibition by compound **3** is much weaker than that of its analogue **1** for both considered substrates. Additionally, inhibitor **3** does not exhibit substrate selectivity because the distances from the oxygen atom of the Fe(III)–OH^{2+} cofactor to the reactive carbon atom and its corresponding hydrogen atoms are very similar for both substrates. It is worth noticing that although H13proR of AA is slightly closer than the corresponding hydrogen atoms of C11 in LA, its H13proS is more distanced than these hydrogen atoms in LA. Notably, considering only the distance criterion, one might suggest that compound **3** slightly activates AA since the reactive carbon atom and its hydrogen atoms are slightly closer to the oxygen atom of the Fe(III)–OH^{2+} cofactor than in the absence of the inhibitor. However, the percentage of well-oriented structures for hydrogen abstraction, a crucial factor in determining the feasibility of abstraction, indicates that **3** indeed acts as an inhibitor (97.78% without inhibitor *vs.* 82.93% for **3** with respect to AA). Moreover, no activation effect during AA oxygenation was observed experimentally (Fig. 3C). According to the percentage of well-oriented structures for hydrogen abstraction, it can also be concluded that **3** does not exhibit significant substrate selectivity and is comparable with the reference compound **1** regarding AA inhibition and much weaker regarding LA inhibition.

3. Experimental

3.1 General

The solvents and reagents were purchased from Acros (Geel, Belgium) or Sigma-Aldrich (Schnelldorf, Germany) and were used without further purification unless otherwise noted. ^{1}H and ^{13}C NMR spectra were recorded using a 300 MHz Brucker MSL spectrometer in $CDCl_3$, acetone-d_6 or DMSO-d_6. Tetramethylsilane was used as the internal standard for ^{1}H-NMR. Chemical shifts in ^{13}C-NMR were referenced to the residual carbon signal of $CDCl_3$, acetone-d_6 or DMSO-d_6 at δ ^{13}C = 77.16, 206.26 or 39.52 ppm, respectively. Chemical shifts are given in ppm, spin–spin interaction constants in Hz. Column chromatography was carried out using silica gel (Macherey-Nagel, Germany, particle size 63–200 μm) as a stationary phase. Silica gel 60 F254 plates (Merck, Germany) were used for thin-layer chromatography (TLC). Compounds were detected under UV light or after staining with an ethanolic (3%) solution of vanillin. Preparative HPLC was performed using a Knauer HPLC pump 64 system coupled with a differential refractometer, UV-vis detector (Knauer, Germany) and equipped with a Luna C18(2), 100A column (75 × 30 mm, 5 μm particle size) (Phenomenex, USA). Isocratic elution system ACN/THF/H_2O/FA (63 : 7:30 : 0.1 v/v) at a flow rate of 25 mL min^{-1} were applied to achieve the best chromatographic performance. Mass spectra (EI) were recorded on an Agilent a 6890N gas chromatograph coupled with 5973N mass spectral detector (Agilent, Santa Clara, CA, USA) using a DB-5ms column (30 m, coating thickness 0.5 μm, Agilent J&W, Palo Alto, CA, USA). An injector temperature of 300 °C, an ion source temperature of 230 °C and the electron energy of 70 eV were set. Helium was used as carrier gas at a flow rate of 1 mL min^{-1}. Samples were eluted using the following temperature program: isothermally at 70 °C for 5 min, then from 70 to 290 °C at a rate of 30 °C min^{-1}, followed by isothermal step at 290 °C for 10 min. Finally, the column was conditioned at 310 °C for 10 min. Analytical HPLC was performed on Agilent 1260 Infinity II instrument (Agilent, China)

Table 3 Relevant average distances for hydrogen abstraction and the percentage of well-oriented structures observed for AA during MD simulations of the AA:ALOX15, **3**(2):AA:ALOX15, and **1**:AA:ALOX15 complexes

System	$d(C_{13}–OH)$ (Å)	$d(H_{13proS}–OH)$ (Å)	$d(H_{13proR}–OH)$ (Å)	Percentage of well-oriented structures
Without inhibitor	5.2	4.8	5.5	97.78
3 [a]	4.9	5.5	4.6	82.93
1	6.4	6.0	7.0	87.90

[a] The MD simulation of the **3**(2):AA:15-LOX complex was extended by additional 200 ns to ensure convergence of the considered magnitudes.

equipped with a PoroShell 300 SB C18 column (75 × 2.1 mm, 5 μm particle size) (Agilent, USA). Gradient elution system composed of solvents A (H_2O with 0.1% formic acid and 10 mM ammonium formiate) and B (ACN with 0.1% formic acid) at a flow rate of 0.6 mL min^{-1} was used. Samples were eluted starting from 5% of system B at increasing system B concentrations followed up isocratic elution at 100% after 10 min. HRMS spectra were obtained on a Waters Synapt XS HDMS mass spectrometer using electrospray ionization in a positive ionization mode (ESI). The interface capillary voltage was set up at 2200 V, and the mass range was from *m*/*z* 50 to 3000 Da. External or internal calibration was performed with electrospray calibration solution kit (Fluka). N_2 was applied as a drying gas. IR spectra were recorded using a Infraspec FSM-2202 FTIR spectrometer (Russia). UV-spectra were recorded using Shimadzu UV-1800 spectrophotometer (Shimadzu, Japan).

3.2 Chemical synthesis

3.2.1 1-(4-Methoxy-3-nitrophenyl)ethan-1-one oxime (5). Compound **4** (1.95 g, 10 mmol), $NH_2OH \cdot HCl$ (1.04 g, 15 mmol) and NaOAc (3.40 g, 20 mmol) were added to a mixture of EtOH (15 mL) and H_2O (50 mL). After the mixture was stirred for 1 h under reflux, it was cooled down to 4 °C, the precipitate was filtered off and washed with cold H_2O (2 × 10 mL). The product was recrystallized twice from H_2O/EtOH mixture (1 : 1, v/v) and dried under reduced pressure. Yield of compound **5**: 90% (1.89 g). TLC: R_f 0.40 (Pet/EtOAc 7 : 3, v/v). Melting point 139–140 °C. IR (KBr): ν 3506 cm^{-1} (s), 1534 cm^{-1} (s), 1355 cm^{-1} (s), 1278 cm^{-1} (s). ^{1}H NMR (300 MHz, $CDCl_3$) δ 8.67 (s, 1H), 8.11 (d, J = 2.32 Hz, 1H), 7.84 (dd, J = 8.84, 2.34 Hz, 1H), 7.10 (d, J = 8.87 Hz, 1H), 3.99 (s, 3H), 2.28 (s, 3H). ^{13}C NMR (75 MHz, $CDCl_3$) δ 153.94, 153.60, 139.52, 131.59, 129.10, 123.56, 113.62, 56.81, 12.00. MS (EI, 70 eV) *m*/*z* (%): 210 (100), 77 (23), 146 (21), 117 (20).

3.2.2 Diphenyliodonium triflate (6). Iodine (0.60 g, 2.40 mmol) was added to a high pressure glass bottle with a solution of mCPBA (1.24 g, 7.20 mmol) in DCM (20 mL). After the mixture was cooled to 0 °C dry benzene (0.88 mL, 9.84 mmol) followed by TfOH (0.82 mL, 9.20 mmol) were added the yellow-coloured mixture was stirred for 10 min at 80 °C and then cooled down to rt. The reaction was quenched with Et_2O (20 mL) and additionally stirred for 10 min at rt. The reaction bottle was then cooled down to −20 °C, kept for 30 min at this temperature, the solid was filtered off, washed with cold Et_2O (3 × 10 mL) and dried under reduced pressure. Yield of compound **6**: 91% (0.94 g). Melting point 173–174 °C (lit. 170–176 °C[25]). ^{1}H NMR (300 MHz, DMSO-d_6) δ 8.30–8.19 (m, 4H), 7.70–7.63 (m, 2H), 7.57–7.50 (m, 4H).

3.2.3 1-(4-Methoxy-3-nitrophenyl)ethan-1-one *O*-phenyl oxime (7). ^{t}BuOK (0.25 g, 2.25 mmol) was added to a solution of 1-(4-methoxy-3-nitrophenyl)ethan-1-one oxime (**5**) (0.32 g, 1.50 mmol) in DMF (15 mL). After the mixture was stirred for 5 min, diphenyliodonium triflate (**6**) (0.97 g, 2.25 mmol) was added. The reaction mixture was stirred for 1.5 h at rt, then quenched with H_2O (75 mL). The organic compounds were extracted with EtOAc (3 × 30 mL). Combined organic layers were washed with brine (50 mL), dried over Na_2SO_4 and evaporated. After purification on silica gel using a gradient elution (Pet/DCM from 2 : 0 to 2 : 1, v/v) compound **7** was obtained in a yield: 74% (0.31 g). TLC: R_f 0.82 (DCM). IR (KBr): ν 1356 cm^{-1} (s), 1324 cm^{-1} (s), 1281 cm^{-1} (s). ^{1}H NMR (300 MHz, $CDCl_3$) δ 8.25 (d, J = 2.29 Hz, 1H), 8.01 (dd, J = 8.84, 2.30 Hz, 1H), 7.39–7.31 (m, 2H), 7.31–7.24 (m, 2H), 7.13 (d, J = 8.90 Hz, 1H), 7.10–7.01 (m, 1H), 4.01 (s, 3H), 2.45 (s, 3H). ^{13}C NMR (75 MHz, $CDCl_3$) δ 159.48, 155.30, 153.93, 153.58, 139.78, 131.91, 129.48, 128.66, 126.24, 123.83, 122.65, 114.94, 113.65, 56.86, 13.08. MS (EI, 70 eV) *m*/*z* (%): 286 (100), 271 (79), 224 (42), 196 (22).

3.2.4 2-(4-Methoxy-3-nitrophenyl)benzofuran (8). To a solution of compound **7** (0.18 g, 0.63 mmol) in dioxane (6 mL) 36% aq. HCl (0.27 mL) was added. The mixture was stirred for 5.5 h under reflux, then cooled down and alkalinized with aq. NH_3 to pH 10. The organic compounds were extracted with DCM (2 × 50 mL). Combined extracts were dried over Na_2SO_4 and evaporated under the reduced pressure. The crude product was purified on silica gel in DCM to give 0.13 g (77%) of compound **8**. TLC: R_f 0.88 (DCM). IR (KBr): ν 1352 cm^{-1} (s), 1277 cm^{-1} (s), 1016 cm^{-1} (s). ^{1}H NMR (300 MHz, $CDCl_3$) δ 8.31 (d, J = 2.25 Hz, 1H), 7.98 (dd, J = 8.79, 2.26 Hz, 1H), 7.58 (dm, J = 7.41 Hz, 1H), 7.51 (dm, J = 8.32 Hz, 1H), 7.34–7.21 (m, 2H), 7.15 (d, J = 8.83 Hz, 1H), 6.98 (d, J = 0.95 Hz, 1H), 4.00 (s, 3H). ^{13}C NMR (75 MHz, $CDCl_3$) δ 155.04, 153.38, 152.91, 140.12, 130.29, 129.08, 124.88, 123.66, 123.40, 122.25, 121.21, 114.13, 111.34, 101.88, 56.86. MS (EI, 70 eV) *m*/*z* (%): 269 (100), 165 (44), 193 (17), 152 (14).

3.2.5 2-(3-Amino-4-methoxyphenyl)benzofuran (9). To a solution of 2-(4-methoxy-3-nitrophenyl)benzofuran (**8**) (0.10 g, 0.37 mmol) in 5 mL MeOH iron powder (0.06 g, 1.11 mmol) was added followed by dropwise addition of 36% aq. HCl (0.37 mL). The mixture was stirred for 3 h at 60 °C, than cooled down to rt and alkalinized with aq. 25% NH_3 (2 mL). The brown precipitate was filtered off through the Celite, the filtrate was diluted with H_2O (10 mL), and the organic compounds were extracted with DCM (3 × 15 mL). The combined organic extracts were dried by passing through Na_2SO_4 and evaporated. The crude product was purified on silica gel in DCM to yield **9**: 90% (0.08 g). TLC: R_f 0.54 (DCM). Analytical HPLC: R_t = 7.43 min (235 nm). IR (KBr): ν 1243 cm^{-1} (s), 1176 cm^{-1} (s). UV/vis λ_{max} 228, 306 nm. ^{1}H NMR (300 MHz, $CDCl_3$) δ 7.56 (dm, J = 8.29 Hz, 1H), 7.50 (dm, J = 8.93 Hz, 1H), 7.30–7.19 (m, 4H), 6.88–6.86 (m, 2H), 3.92 (s, 3H). ^{13}C NMR (75 MHz, $CDCl_3$) δ 156.52, 154.74, 147.99, 136.80, 136.43, 129.65, 123.72, 122.86, 120.62, 115.86, 111.51, 111.05, 110.53, 99.75, 55.69. MS (EI 70 eV) *m*/*z* (%): 224 (100), 239 (71), 196 (33).

3.2.6 Octyl (*N*-(4-(benzofuran-2-yl)-2-methoxyphenyl) sulfamoyl)-carbamate (2). Chlorosulfanyl isocyanate (36.50 μL, 0.42 mmol) was added to a solution of octanol-1 (47.50 μL, 0.30 mmol) in dry DCM (1 mL). The mixture was stirred at for 15 min at rt, then TEA (63 mL, 0.45 mmol) was added and the mixture was additionally stirred for 15 min. Finally, a solution of 2-(3-amino-4-methoxyphenyl)benzofuran (**9**) (40 mg, 0.17 mmol) in dry DCM (0.5 mL) was added and the resulting mixture was stirred for 3 h at rt, quenched with H_2O (1.5 mL), the organic layer was separated, dried with Na_2SO_4 and concentrated *in*

vacuo. The raw product was purified on silica gel (THF/Pet 1 : 2, v/v) followed by preparative RP-HPLC to yield compound **2**: 54% (43 mg). TLC: R_f 0.54 (THF/Pet 1 : 2, v/v). Analytical HPLC: R_t = 10.02 min (235 nm). UV/vis λ_{max} 229, 307 nm. ^{1}H NMR (300 MHz, $CDCl_3$) δ 7.98 (d, J = 2.09 Hz, 1H), 7.62 (dd, J = 8.56, 2.11 Hz, 2H), 7.58–7.46 (m, 2H), 7.31–7.17 (m, 2H), 6.96–6.90 (m, 2H), 4.12 (t, J = 6.75 Hz, 2H), 3.89 (s, 3H), 1.58 (p, J = 6.89 Hz, 2H), 1.32–1.16 (m, 10H), 0.86 (t, J = 6.50 Hz, 3H). ^{13}C NMR (75 MHz, $CDCl_3$) δ 155.19, 154.96, 150.78, 149.67, 129.42, 126.03, 124.27, 123.49, 123.11, 122.46, 120.91, 116.99, 111.30, 111.25, 100.93, 67.48, 56.27, 31.85, 29.24, 29.21, 28.58, 25.71, 22.73, 14.17. HRMS (ESI): found: 475.1897, error ppm = 0.21, calculated for single-charged ions [M + H] with formula $C_{24}H_{31}N_2O_6S^{1+}$: 475.1898.

3.2.7 3-Methoxy-4-nitrobenzoyl chloride (11). To a suspension of 3-methoxy-4-nitrobenzoic acid (4.00 g, 20 mmol) in toluene (27 mL) $SOCl_2$ (2.20 mL, 30 mmol) and DMF (30.0 μL) were added. The mixture was stirred for 1 h under reflux, then concentrated *in vacuo* and washed with pet (2 × 5 mL). Yield of raw **11**: 95% (4.15 g). MS (EI, 70 eV) *m*/*z* (%): 180 (100), 215 (14), 217 (5).

3.2.8 *N*,3-Dimethoxy-*N*-methyl-4-nitrobenzamide (12). To the ice-cooled suspension of *N*,*O*-dimethylhydroxylamine hydrochloride (0.46 g, 4.70 mmol) in dry DCM (4 mL) TEA (1.32 mL, 9.40 mmol) was added. After that a solution of 3-methoxy-4-nitrobenzoyl chloride **11** (1.02 g, 4.70 mmol) in dry DCM (25 mL) was added to the reaction and the mixture was stirred overnight at rt, then quenched with saturated $NaHCO_3$ solution (25 mL), washed with brine (20 mL) and H_2O (20 mL), dried with Na_2SO_4 and evaporated. The raw product was purified on silica gel with DCM to yield 78% (0.88 g) of **12**. TLC: R_f 0.33 (DCM). IR (KBr): ν 1717 cm^{-1} (v.s), 1120 cm^{-1} (s). ^{1}H NMR (300 MHz, acetone-d_6) δ 7.86 (d, J = 8.32 Hz, 1H), 7.49 (s, 1H), 7.32 (d, J = 8.29 Hz, 1H), 4.01 (s, 3H), 3.61 (s, 3H), 3.30 (s, 3H). ^{13}C NMR (75 MHz, acetone-d_6) δ 165.30, 152.98, 143.82, 136.13, 125.77, 122.24, 115.47, 62.52, 57.38, 14.54. MS (EI, 70 eV) *m*/*z* (%): 180 (100), 133 (20), 122 (16), 240 (10).

3.2.9 Diethyl 3-methoxy-4-nitrobenzoylmalonate (14). To a dry two-necked round-bottomed flask equipped with Dimroth condenser, PTFE/silicone septum and magnetic stirrer filled with magnesium turnings (0.50 g, 20 mmol) a mixture of absolute EtOH (0.46 mL), CCl_4 (46 μL), and dry Et_2O (14 mL) was added under argon. Finally, a mixture of diethyl malonate (3.28 g, 20 mmol), absolute EtOH (1.85 mL) and dry Et_2O (2.30 mL) was added to the reaction flask so that the rapid boiling could be maintained. The mixture was refluxed for 3 h until the magnesium turnings were completely dissolved. To a grey suspension formed a solution of 3-methoxy-4-nitrobenzoyl chloride **11** (3.99 g, 18.5 mmol) in dry Et_2O (15 mL) was added over 15 min followed by the compound **12**. The reaction mixture was additionally refluxed until the yellowish viscous suspension was formed, cooled down and quenched with 11% aq. H_2SO_4 (19 mL) until the solid was dissolved. The organic phase was separated and the organic products were extracted with Et_2O (4 × 40 mL). The combined extracts were washed with H_2O (100 mL), and the solvent was removed under reduced pressure. The crude product **14** (5.87 g) was used in the next stage without further purification. TLC: R_f 0.5 (Pet/EA 7 : 3, v/v).

3.2.10 1-(3-Methoxy-4-nitrophenyl)ethan-1-one (15). To the crude diethyl 3-methoxy-4-nitrobenzoylmalonate (**14**) (5.87 g) a mixture of glacial AcOH (5.56 mL), H_2SO_4 (0.70 mL), and H_2O (3.70 mL) was added. The resulting mixture was stirred for 3.5 h under reflux and the reaction progress was monitored by TLC. After the reaction was complete, the mixture was cooled down, alkalinized by addition of 20% aq. NaOH (15 mL) and organic compounds were extracted with Et_2O (5 × 20 mL). The combined ethereal extracts were washed with H_2O (80 mL), dried over Na_2SO_4, and the solvent was removed under reduced pressure. The purification on silica gel using a gradient elution (Pet/EA 9 : 1 to 7 : 3, v/v) gave 1.32 g (36.5%) 1-(3-methoxy-4-nitrophenyl)ethan-1-one (**15**). TLC: R_f 0.41 (Pet/EA 7 : 3, v/v). IR (KBr): ν 1685 cm^{-1} (v.s), 1354 cm^{-1} (s), 1287 cm^{-1} (s). ^{1}H NMR (300 MHz, $CDCl_3$) δ 7.84 (d, J = 8.30 Hz, 1H), 7.66 (s, 1H), 7.55 (d, J = 8.24 Hz, 1H), 4.00 (s, 3H), 2.63 (s, 3H). ^{13}C NMR (75 MHz, $CDCl_3$) δ 196.36, 152.82, 141.10, 125.74, 120.58, 112.74, 56.83, 26.96. MS (EI, 70 eV) *m*/*z* (%): 180 (100), 195 (62), 133 (23), 122 (22).

3.2.11 1-(4-Amino-3-methoxyphenyl)ethan-1-one (16). To a solution of **15** (100 mg, 0.51 mmol) in methanol (1.5 mL) iron powder 86 mg (1.5 mmol) and concentrated aq. HCl (0.5 mL) were added. The mixture was stirred for 1 h at 60 °C and the reaction progress was monitored by TLC. After the reaction was complete, the mixture was alkalinized with 25% aq. NH_3 (1 mL), the solid was filtered off and the organic products were extracted with DCM (3 × 5 mL). The DCM extracts were passed through Na_2SO_4 and solvent was removed under reduced pressure. The product was used in the next steps without further purification yield of **16**: 87% (74 mg). TLC: R_f 0.16 (DCM). IR (KBr): ν 3432 cm^{-1} (s), 3323 cm^{-1} (s), 1643 cm^{-1} (v.s), 1262 cm^{-1} (s). ^{1}H NMR (300 MHz, $CDCl_3$) δ 7.48–7.43 (m, 2H), 6.65 (d, J = 8.57 Hz, 1H), 4.29 (s, 2H), 3.91 (s, 3H), 2.52 (s, 3H). ^{13}C NMR (75 MHz, $CDCl_3$) δ 196.59, 146.55, 141.85, 127.91, 124.26, 112.62, 109.38, 55.65, 26.03. MS (EI, 70 eV) *m*/*z* (%): 150 (100), 165 (62), 122 (14).

3.2.12 4-(1*H*-Indol-2-yl)-2-methoxyaniline (17). A mixture of 80% polyphosphoric acid (500 mg), phenylhydrazine (145 mg 1 mmol) and ketone **16** (165 mg, 1 mmol) was kept for 20 minutes at 130 °C. After the reaction mixture was cooled down, it was quenched with ice-cold H_2O (2 mL) and alkalized with 25% aq. NH_3 (4 mL). The precipitate was separated and dissolved in DCM (10 mL), the solution was dried through Na_2SO_4, and the solvent was removed under reduced pressure. The raw product was purified on silica gel with DCM. Yield of **17**: 28% (67 mg). TLC: R_f 0.65 (THF/Pet 2 : 1, v/v). Analytical HPLC: R_t = 4.99 min (235 nm). IR (KBr): ν 3438 cm^{-1} (s), 1625 cm^{-1} (s), 1289 cm^{-1} (s), 1220 cm^{-1} (s), 1021 cm^{-1} (s). UV/vis λ_{max} 231, 331 nm. ^{1}H NMR (300 MHz, DMSO-d_6) δ 11.24 (s, 1H), 7.44 (dm, J = 7.65 Hz, 1H), 7.37–7.29 (m, 2H), 7.22 (dm, J = 8.04, 1H), 7.08–6.88 (m, 2H), 6.74–6.62 (m, 2H), 4.94 (s, 2H), 3.88 (s, 3H). ^{13}C NMR (75 MHz, DMSO-d_6) δ 146.63, 139.18, 137.09, 136.72, 129.07, 120.96, 120.48, 119.25, 119.05, 118.23, 114.03, 110.78, 107.84, 96.09, 55.52. MS (EI, 70 eV) *m*/*z* (%): 238 (100), 195 (59), 223 (16), 97 (15), 119 (12).

3.2.13 Octyl (*N*-(4-(1*H*-indol-2-yl)-2-methoxyphenyl) sulfamoyl)-carbamate (3). Compound **3** was prepared from octanol-1 (56.9 μL, 0.36 mmol), chlorosulfanyl isocyanate (43.5

μL, 0.50 mmol), TEA (75 μL, 0.54 mmol) and 4-(1*H*-indol-2-yl)-2-methoxyaniline (**18**) (48 mg, 0.2 mmol) as described for compound **2**. The raw product was purified on silica gel (THF/Pet 1 : 2, v/v) followed by preparative RP-HPLC to give 55 mg (58%) of compound **3**. TLC: R_f 0.76 (THF/Pet 2 : 1, v/v). Analytical HPLC: R_t = 7.08 min (235 nm). UV/vis λ_{max} 229, 326 nm. ^{1}H NMR (300 MHz, acetone-d_6) δ 10.66 (s, 1H), 7.57–7.51 (m, 3H), 7.46 (dd, J = 8.36, 1.84 Hz, 1H), 7.39 (dd, J = 8.07, 0.95 Hz, 1H), 7.13–7.06 (m, 1H), 7.04–6.98 (m, 1H), 6.92–6.89 (m, 1H), 4.12 (t, J = 6.61 Hz, 2H), 4.01 (s, 3H), 1.59 (p, J = 6.94 Hz, 2H), 1.32–1.18 (m, 10H), 0.82 (t, J = 6.22 Hz, 3H). ^{13}C NMR (75 MHz, acetone-d_6) δ 151.79, 151.63, 138.37, 131.37, 130.30, 126.28, 123.93, 123.89, 122.80, 122.34, 121.17, 120.62, 118.52, 112.06, 112.01, 109.26, 100.25, 100.20, 67.13, 56.83, 32.59, 26.47, 23.35, 14.39. HRMS (ESI): found: 474.2064, error ppm = 1.26, calculated for single-charged ions [M + H] with formula $C_{24}H_{32}N_3O_5S^{1+}$: 474.2058.

3.3 Enzyme preparation

Wild-type rabbit ALOX15 was expressed as *N*-terminal His-tag fusion proteins in *E. coli*[20] and purified as described previously.[26] Typically, an electrophoretic purity >95% of the enzyme preparation was reached. Additionally, the enzyme preparation was tested for product specificity with AA or LA. For this purpose the purified enzyme (2–10 μL) was incubated with AA or LA (25 μM) in PBS for 3 min at 25 °C. The reaction was stopped by the addition of $NaBH_4$. Samples were acidified, protein was precipitated by the addition of 0.5 mL of acetonitrile and the precipitate was spun down. The product specificity for AA oxygenation was measured by HPLC (formation of 12- + 15-HETE) (Fig. S2).

3.4 ALOX15 activity assay

The impact of inhibitors on the rate of LA or AA oxygenation (25 μM final concentrations, the stock prepared as Na^+-salt in PBS) was assayed spectrophotometrically measuring the increase in conjugated diene formation (235 nm). The assay mixture was composed of a 0.1 M PBS at pH 7.4 and various concentrations of inhibitors. No detergent was used. The compounds **2** and **3** were reconstituted in DMSO and serial dilutions were carried out so that from each dilution 1 μL was applied for the measurement. Purified rabbit ALOX15 (5 μg) was pre incubated with a testing compound for 1 min and the reaction was started by the addition of the substrate. The linear part of the kinetic progress curve was evaluated. The activity of the solvent controls (1 μL DMSO) was set as 100%.

3.5 Molecular docking studies

Docking studies were carried out with the program GOLD5.8.0.[27] A thorough conformational exploration was performed for each considered ligand inside its putative cavity, calculating 1000 different poses in each case, which were clustered subsequently. Concerning the inhibitor compound **3**, the calculations were restricted to the binding cavity of monomer A of rabbit ALOX15, considering the crystallographic X-ray structure of the dimeric enzyme (PDB entry 2P0M) as the receptor.[17] Prior to initiating the docking protocol, the ligand bound at the active site of the crystal structure was removed. Hydrogen coordinates were generated with the H++ web server[28,29] using a pH 6.0 for titrable residues. In contrast, regarding substrates, AA and LA docking calculations were restricted to the binding cavity of monomer B of rabbit ALOX15, considering the relaxed **3**(1):ALOX15 and **3**(2):ALOX15 complexes, *i.e.*, the last structure of their MD simulations, as the receptors. The binding site cavity used in the docking runs is a 20 Å radius sphere centered around the iron atom of monomer A, when the inhibitor compound **3** acts as the ligand, or the iron atom of monomer B when substrates AA or LA acts as the ligand. The receptor was kept frozen, but complete flexibility was given to the considered ligand in the conformational search. The GOLD option to consider interactions of organic ligands with metal ions in metalloenzymes was activated, though the docking exploration was limited to iron hexacoordinated geometries. The most efficient genetic algorithm was used to ensure an extensive search of the conformational space of all substrates. To estimate the binding free energies of substrates, the ChemScore scoring function has been selected.

3.6 Molecular dynamics simulations

The different systems were assembled using the procedure recommended by the AMBER software package.[30] The ff14SB[31] force field was used for the protein atoms, while the force field parameters for AA,[32] LA,[33] and iron along with its first coordination sphere[21] (His361, His366, His541, His545, Ile663 and OH^-) were taken from previous works. Additionally, the specific parameters of compound **3** were developed here. The calculations to generate those specific parameters were carried out following the standard protocol in AMBER with antechamber and parmchk2 modules. The GAFF2 (ref. 34) library was used as the source for all these parameters. The B3LYP/6-31G(d) level of theory was employed to optimize the structure of compound **3** and its atomic charges were assigned using the Merz–Kollman RESP procedure.[35] Finally, the protonation states of all considered ligands were established by hand to ensure that they matched the protonation states under physiological conditions.

All MD simulations followed the same protocol, being the only difference the starting structures. It is worth noting that the **3**(1):ALOX15 MD simulation was enlarged 100 additional ns to ensure the stability of such binding mode of compound **3**, while the **3**(2):AA:15-LOX MD simulation was extended by additional 200 ns to ensure the convergence of the considered magnitudes regarding the AA reactivity. After combining the corresponding files, the different complexes were solvated with an orthorhombic box of pre-equilibrated TIP3P waters[36] and their total charge was neutralized by adding sodium cations using the tLeap program. The resulting systems contain nearly 200 000 atoms, about 21 000 of them being protein atoms. The remaining atoms represent water molecules and salt ions. All molecular dynamics (MD) simulations were run with the AMBER 22 GPU (CUDA) version of the PMEMD package.[37,38] Initially, the system was submitted to 22 000 energy minimization steps using the steepest-descent method to avoid close contacts. In the first 6000 steps, harmonic restraints were applied to the protein and ligand (inhibitor and/or substrate) atoms with a force constant of 5.0 kcal mol^{-1} Å^{-2}, so that

solvent and ions were relaxed exclusively. In the next 6000 steps, harmonic restraints were applied to the protein backbone and the ligand heavy atoms with a force constant of 5.0 kcal mol^{-1} $Å^{-2}$. In the last 10 000 steps, the entire system was kept free of restraints. After that, MD simulations using periodic boundary conditions were carried out. The system was gradually heated from 0 to 300 K for a period of 200 ps. Next, an MD run of 1 ns, at constant temperature and pressure (300 K, 1 bar), has been calculated to adjust the volume of the orthorhombic box so that a density of around 1 g cm^{-3} is reached. Throughout the heating and compressing, harmonic restraints were applied to the protein backbone and ligand heavy atoms with a force constant of 5.0 kcal mol^{-1} $Å^{-2}$, whereas no restraints were applied to the rest of the system. The temperature was controlled by Langevin dynamics,[39] while the pressure was adjusted by the Berendsen barostat.[40] Then, an equilibration stage of 10 ns, at constant temperature (300 K) and volume, was carried out. Finally, a production period of 200 ns was run within the same isothermal–isochoric ensemble. As in previous works, this length for the production period turned out to be adequate for letting protein–inhibitor and protein–inhibitor–substrate complexes relax and adapt to the presence of the corresponding added ligand. A time step of 2 fs was used along the whole MD trajectory. All bonds and bends containing hydrogen atoms were constrained by the SHAKE algorithm.[41] Nonbonding interactions have been calculated with a cutoff of 9 Å. The best docking solution of the two best clusters of the inhibitor compound **3** (**3**(1) and **3**(2)) along with the aforementioned processed structure of the dimeric rabbit ALOX15 were used as the starting structures for the MD simulations of the **3**(1):ALOX15 and **3**(2):ALOX15 complexes. On the other hand, the best docking solution of the best cluster of AA and LA into the cavity of monomer B for the last structure of the MD simulations of the **3**(1):ALOX15 and **3**(2):ALOX15 complexes, compatible with their experimentally observed reactivity, along with such structures of given complexes were taken to initiate the MD simulations of the **3**(1):AA/LA:ALOX15 and **3**(2):AA/LA:ALOX15 complexes. For the sake of comparison, we have also included the results of the MD simulations of the AA/LA:ALOX15 and **1**:AA/LA:ALOX15 complexes from our previous studies. Analysis of the MD simulations was carried out with AmberTools, whereas visualization of those trajectories was performed with VMD[42] and USCF CHIMERA[43] programs.

4. Conclusions

Based on theoretical and experimental data, it can be concluded that:

(1) NH to O exchange in the main core pharmacophore (compound **2**) reduces the degree of substrate specificity (IC_{50}(LA)/IC_{50}(AA) value) of ALOX15 inhibition but does not eliminate this effect.

(2) Compound **3** binds to the allosteric ALOX15-substrate complex, but does not induce any substrate selective enzyme inhibition. It also has lower inhibitor potency when compared with its analogue **1**.

(3) A swap of the substituents at the core of inhibitor **3** leads to a loss of the interaction between its SO_2 group and the side chain NH_2-group of Gln596 in the ALOX15–inhibitor complex suggesting a crucial role of this interaction for substrate specific ALOX15 inhibition.

(4) As indicated by MD simulations fatty acid binding in the substrate binding pocket of monomer B of the ALOX15-inhibitor complex forces the inhibitor to adopt a different position in the substrate binding pocket of monomer A.

Author contributions

Conceptualization, I.I., V.G., A.Zh., H.K., A.C., J.M.L., and A.G.L.; investigation, V.G., A.Zh., A.C., A.G., V.A., D.N.; writing—original draft preparation, V.G., A.Zh., I.I., H.K., A.C., J.M.L. and A.G.L; writing—review and editing, I.I., A.G.L., J.M.L. and H.K.; funding acquisition, I.I., A.G.L., J.M.L and H.K. All authors have read and agreed to the published version of the manuscript.

Conflicts of interest

No conflict of interest to be declared. The funders had no role in the design of the study or in the decision to publish the results.

Data availability

The dataset for this publication can be found in: **https://dataverse.csuc.cat/dataverse/UAB** with the persistent DOI: **https://doi.org/10.34810/data2491**.

Supplementary information: SI tables and figures, ^{1}H-, ^{13}C-NMR, IR, UV-spectra, chromatograms. Inhibitor:protein interactions. See DOI: **https://doi.org/10.1039/d5ra03640b**.

Acknowledgements

Russian Ministry of Science and High Education (FSFZ-2023-0004) supported the experimental part of this work. We thank the Spanish "Ministerio de Ciencia, Innovación y Universidades" (Grant PID2020-113764GB-I00 and Grant PID2023-147140NB-I00). We also acknowledge CSUC for computational facilities as well as a Shared Science and training Center for Collective Use of RTU MIREA supported by the Ministry of Science and Higher Education by Agreement No. 075-15-2025-548.

References

1 G. P. Pidgeon, J. Lysaght, S. Krishnamoorthy, J. V. Reynolds, K. O'Byrne, D. Nie and K. V. Honn, *Cancer Metastasis Rev.*, 2007, **26**, 503–524.
2 I. Cimen, S. Tuncay and S. Banerjee, *Cancer Sci.*, 2009, **100**, 2283–2291.
3 N. Mochizuki and Y. G. Kwon, *Circ. Res.*, 2008, **102**, 143–145.
4 L. Zhao, T. Grosser, S. Fries, L. Kadakia, H. Wang, J. Zhao and R. Falotico, *Expert Rev. Clin. Immunol.*, 2006, **2**, 649–658.
5 A. A. Kapralov, Q. Yang, H. H. Dar, Y. Y. Tyurina, T. S. Anthonymuthu, R. Kim, C. M. St. Croix, K. Mikulska-

Ruminska, B. Liu, I. H. Shrivastava, V. A. Tyurin, H.-C. Ting, Y. L. Wu, Y. Gao, G. V. Shurin, M. A. Artyukhova, L. A. Ponomareva, P. S. Timashev, R. M. Domingues, D. A. Stoyanovsky, J. S. Greenberger, R. K. Mallampalli, I. Bahar, D. I. Gabrilovich, H. Bayır and V. E. Kagan, *Nat. Chem. Biol.*, 2020, **16**, 278–290.

6 D. D. Sears, P. D. Miles, J. Chapman, J. M. Ofrecio, F. Almazan, D. Thapar and Y. I. Miller, *PLoS One*, 2009, **4**, e7250.

7 D. C. Lieb, J. J. Brotman, M. A. Hatcher, M. S. Aye, B. K. Cole, B. A. Haynes, S. D. Wohlgemuth, M. A. Fontana, H. Beydoun, J. L. Nadler and A. D. Dobrian, *J. Clin. Endocrinol. Metab.*, 2014, **99**, E1713–E1720.

8 V. Vangaveti, V. Shashidhar, F. Collier, J. Hodge, C. Rush, U. Malabu, B. Baune and R. L. Kennedy, *Therap. Adv. Endocrinol. Metabol.*, 2018, **9**, 137–150.

9 R. A. Daynes and D. C. Jones, *Nat. Rev. Immunol.*, 2002, **2**, 748–759.

10 G. Kronke, J. Katzenbeisser, S. Uderhardt, M. M. Zaiss, C. Scholtysek, G. Schabbauer, A. Zarbock, M. I. Koenders, R. Axmann, J. Zwerina, H. W. Baenckler, W. van den Berg, R. E. Voll, H. Kuhn, L. A. Joosten and G. Schett, *J. Immunol.*, 2009, **183**, 3383–3389.

11 E. Sigal, C. S. Craik, E. Highland, D. Grunberger, L. L. Costello, R. A. Dixon and J. A. Nadel, *Biochem. Biophys. Res. Commun.*, 1988, **157**, 457–464.

12 H. Kuhn, H. Sprecher and A. R. Brash, *J. Biol. Chem.*, 1990, **265**, 16300–16305.

13 J. P. Klinman, A. R. Offenbacher and S. Hu, *J. Am. Chem. Soc.*, 2017, **139**, 18409–18427.

14 A. T. Wecksler, V. Kenyon, J. D. Deschamps and T. R. Holman, *Biochemistry*, 2008, **47**, 7364–7375.

15 D. S. Weinstein, W. Liu, K. Ngu, C. Langevine, D. W. Combs, S. Zhuang, C. Chen, C. S. Madsen, T. W. Harper and J. A. Robl, *Bioorg. Med. Chem. Lett.*, 2007, **17**, 5115–5120.

16 A. Golovanov, A. Zhuravlev, A. Cruz, V. Aksenov, R. Shafiullina, K. R. Kakularam, J. M. Lluch, H. Kuhn, A. Gonzalez-Lafont and I. Ivanov, *J. Med. Chem.*, 2022, **65**, 1979–1995.

17 J. Choi, J. K. Chon, S. Kim and W. Shin, *Proteins*, 2008, **70**, 1023–1032.

18 W. Shang, I. Ivanov, D. I. Svergun, O. Y. Borbulevych, A. M. Aleem, S. Stehling, J. Jankun, H. Kuhn and E. Skrzypczak-Jankun, *J. Mol. Biol.*, 2011, **409**, 654–668.

19 I. Ivanov, A. Cruz, A. Zhuravlev, A. Di Venere, E. Nicolai, S. Stehling, J. M. Lluch, À. González-Lafont and H. Kuhn, *Int. J. Mol. Sci.*, 2021, **22**, 3285.

20 A. Zhuravlev, A. Cruz, V. Aksenov, A. Golovanov, J. M. Lluch, H. Kuhn, À. González-Lafont and I. Ivanov, *Molecules*, 2023, **28**, 5418.

21 A. Cruz, A. Di Venere, G. Mei, A. Zhuravlev, A. Golovanov, S. Stehling, D. Heydeck, J. M. Lluch, À. González-Lafont, H. Kuhn and I. Ivanov, *Biochim. Biophys. Acta Mol. Cell Biol. Lipids*, 2020, **1865**, 158680.

22 T. R. Holman, J. Zhou and E. I. Solomon, *J. Am. Chem. Soc.*, 1998, **120**, 12564–12572.

23 M. Bielawski, M. Zhu and B. Olofsson, *Adv. Synth. Catal.*, 2007, **349**, 2610–2618.

24 H. Gao, Q. L. Xu, C. Keene and L. Kürti, *Chemistry*, 2014, **20**, 8883–8887.

25 Z. Gonda and Z. Novák, *Chemistry*, 2015, **21**, 16801–16806.

26 I. Ivanov, A. Di Venere, T. Horn, P. Scheerer, E. Nicolai, S. Stehling, C. Richter, E. Skrzypczak-Jankun, G. Mei, M. Maccarrone and H. Kuhn, *Biochim. Biophys. Acta*, 2011, **1811**, 1001–1010.

27 G. Jones, P. Willett, R. C. Glen, A. R. Leach and R. Taylor, *J. Mol. Biol.*, 1997, **267**, 727–748.

28 R. Anandakrishnan, B. Aguilar and A. V. Onufriev, *Nucleic Acids Res.*, 2012, **40**, W537–W541.

29 J. C. Gordon, J. B. Myers, T. Folta, V. Shoja, L. S. Heath and A. Onufriev, *Nucleic Acids Res.*, 2005, **33**, W368–W371.

30 D. A. Case, I. Y. Ben-Shalom, S. R. Brozell, D. S. Cerutti, T. E. Cheatham III, V. W. D. Cruzeiro, T. A. Darden, R. E. Duke, D. Ghoreishi, M. K. Gilson, H. Gohlke, A. W. Goetz, D. Greene, R. Harris, N. Homeyer, S. Izadi, A. Kovalenko, T. Kurtzman, T. S. Lee, S. LeGrand, P. Li, C. Lin, J. Liu, T. Luchko, R. Luo, D. J. Mermelstein, K. M. Merz, Y. Miao, G. Monard, C. Nguyen, H. Nguyen, I. Omelyan, A. Onufriev, F. Pan, R. Qi, D. R. Roe, A. Roitberg, C. Sagui, S. Schott-Verdugo, J. Shen, C. L. Simmerling, J. Smith, R. Salomon-Ferrer, J. Swails, R. C. Walker, J. Wang, H. Wei, R. M. Wolf, X. Wu , L. Xiao, D. M. York and P. A. Kollman, *AMBER 2018*, University of California, San Francisco, 2018.

31 J. A. Maier, C. Martinez, K. Kasavajhala, L. Wickstrom, K. E. Hauser and C. Simmerling, *J. Chem. Theory Comput.*, 2015, **11**, 3696–3713.

32 P. Tosco, *J. Am. Chem. Soc.*, 2013, **135**, 10404–10410.

33 I. Ivanov, A. B. Golovanov, C. Ferretti, M. Canyelles-Niño, D. Heydeck, S. Stehling, J. M. Lluch, À. González-Lafont and H. Kühn, *ACS Chem. Biol.*, 2019, **14**, 2768–2782.

34 J. Wang, R. M. Wolf, J. W. Caldwell, P. A. Kollman and D. A. Case, *J. Comput. Chem.*, 2004, **25**, 1157–1174.

35 C. I. Bayly, P. Cieplak, W. D. Cornell and P. A. Kollman, *J. Phys. Chem.*, 1993, **97**, 10269–10280.

36 W. L. Jorgensen, J. Chandrasekhar, J. D. Madura, R. W. Impey and M. L. Klein, *J. Chem. Phys.*, 1983, **79**, 926–935.

37 R. Salomon-Ferrer, A. W. Gotz, D. Poole, S. Le Grand and R. C. Walker, *J. Chem. Theory Comput.*, 2013, **9**, 3878–3888.

38 S. Le Grand, A. W. Gotz and R. C. Walker, *Comput. Phys. Commun.*, 2013, **184**, 374–380.

39 A. R. Leach, *Molecular Modeling: Principles and Applications*, Eddison Wesley Longman Limited, Essex, England, 1996.

40 H. J. C. Berendsen, J. P. M. Postma, W. F. Vangunsteren, A. Dinola and J. R. Haak, *J. Chem. Phys.*, 1984, **81**, 3684–3690.

41 J. Ryckaert, G. Ciccotti and H. Berendsen, *J. Comput. Phys.*, 1977, **23**, 327–341.

42 W. Humphrey, A. Dalke and K. Schulten, *J. Mol. Graph.*, 1996, **14**(33–38), 27–38.

43 E. F. Pettersen, T. D. Goddard, C. C. Huang, G. S. Couch, D. M. Greenblatt, E. C. Meng and T. E. Ferrin, *J. Comput. Chem.*, 2004, **25**, 1605–1612.